Department of Chemistry Publications   Department of Chemistry

Ice cloud formation potential by free tropospheric particles from long-range transport over the Northern Atlantic Ocean

Swarup China
Michigan Technological University

Peter A. Alpert
Stony Brook University

B. Zhang
Michigan Technological University

Simeon Schum
Michigan Technological University

Katja Dzepina
Michigan Technological University

See next page for additional authors

Recommended Citation

Authors

Swarup China, Peter A. Alpert, B. Zhang, Simeon Schum, Katja Dzepina, Kendra Wright, R. Chris Owen, Paulo Fialho, Lynn Mazzoleni, Claudio Mazzoleni, and Daniel A. Knopf

RESEARCH ARTICLE

Key Points:
- Long-range transported particles in the free troposphere (FT) can promote ice formation
- Ice nucleating particles at a remote FT site are multicomponent and contain organics
- Aged FT particles transported from different locations show similar ice formation potentials

Supporting Information:
- Supporting Information S1

Correspondence to:
S. China and P. A. Alpert,
schina@mtu.edu;
peter.alpert@psi.ch

Ice cloud formation potential by free tropospheric particles from long-range transport over the Northern Atlantic Ocean

Swarup China[1,2,3] (iD), Peter A. Alpert[4,5] (iD), Bo Zhang[1,6] (iD), Simeon Schum[1,7] (iD), Katja Dzepina[7,8] (iD), Kendra Wright[1,2], R. Chris Owen[1,6,9], Paulo Fialho[10] (iD), Lynn R. Mazzoleni[1,7] (iD), Claudio Mazzoleni[1,2] (iD), and Daniel A. Knopf[4] (iD)

[1]Atmospheric Sciences Program, Michigan Technological University, Houghton, Michigan, USA, [2]Department of Physics, Michigan Technological University, Houghton, Michigan, USA, [3]Now at Pacific Northwest National Laboratory, Richland, Washington, USA, [4]Institute for Terrestrial and Planetary Atmospheres, School of Marine and Atmospheric Sciences, Stony Brook University, Stony Brook, New York, USA, [5]Now at Laboratory of Environmental Chemistry, Paul Scherrer Institute, Villigen, Switzerland, [6]Department of Civil and Environmental Engineering, Michigan Technological University, Houghton, Michigan, USA, [7]Department of Chemistry, Michigan Technological University, Houghton, Michigan, USA, [8]Now at Department of Biotechnology, University of Rijeka, Rijeka, Croatia, [9]Now at US Environmental Protection Agency, RTP, North Carolina, USA, [10]Instituto de Investigação em Vulcanologia e Avaliação de Riscos da Universidade dos Açores, Ponta Delgada, Açores, Portugal

Abstract Long-range transported free tropospheric particles can play a significant role on heterogeneous ice nucleation. Using optical and electron microscopy we examine the physicochemical characteristics of ice nucleating particles (INPs). Particles were collected on substrates from the free troposphere at the remote Pico Mountain Observatory in the Azores Islands, after long-range transport and aging over the Atlantic Ocean. We investigate four specific events to study the ice formation potential by the collected particles with different ages and transport patterns. We use single-particle analysis, as well as bulk analysis to characterize particle populations. Both analyses show substantial differences in particle composition between samples from the four events; in addition, single-particle microscopy analysis indicates that most particles are coated by organic material. The identified INPs contained mixtures of dust, aged sea salt and soot, and organic material acquired either at the source or during transport. The temperature and relative humidity (*RH*) at which ice formed, varied only by 5% between samples, despite differences in particle composition, sources, and transport patterns. We hypothesize that this small variation in the onset *RH* may be due to the coating material on the particles. This study underscores and motivates the need to further investigate how long-range transported and atmospherically aged free tropospheric particles impact ice cloud formation.

1. Introduction

Atmospheric ice nucleation directly affects the climate system, Earth's atmosphere, and the hydrological cycle by impacting precipitation, cloud electrification, and atmospheric radiative transfer [*Cantrell and Heymsfield*, 2005]. Greater than 50% of Earth's precipitation originates via the ice phase [*Lau and Wu*, 2003] impacting the global hydrological cycle [*Mülmenstädt et al.*, 2015]. Heterogeneous ice nucleation occurs due to the presence of ice nucleating particles (INPs) that catalyze freezing at warmer temperatures ($>\sim 238$ K) and lower relative humidities with respect to ice ($RH_{ice} < \sim 150–170\%$) than necessary for homogeneous ice nucleation [*Koop et al.*, 2000]. Heterogeneous ice nucleation plays an important role in the formation of mixed-phase clouds (coexistence of supercooled liquid droplets and ice crystals) and cirrus clouds (containing solely ice crystals) by affecting the concentration and shape of ice crystals [*Avramov and Harrington*, 2010; *Morrison et al.*, 2012] and, in turn, it influences atmospheric radiative fluxes and the global energy balance [*Kärcher and Ström*, 2003; *McFarquhar et al.*, 2007].

High-altitude studies point out the complexity and variety of the composition of INPs in the atmosphere. Mineral dust particles were observed in the residuals of evaporated ice crystals in cirrus-forming regions [*Cziczo et al.*, 2013; *Cziczo and Froyd*, 2014] and in the free troposphere at Mount Werner, Colorado, at 3220 m above sea level (asl) [*DeMott et al.*, 2003]. Combinations of natural mineral dust/fly ash and metallic particles were also identified as INPs in natural and anthropogenic air masses [*DeMott et al.*, 2003; *Richardson et al.*, 2007]. Residual biological material from evaporated ice crystals was collected with an

aircraft at high altitude (~8.3 km) over Wyoming [*Pratt et al.*, 2009]. Long-range transported dust and biological particles from the Sahara region were found to be potential INPs over the western United States [*Creamean et al.*, 2013]. Sulfate and organic aerosol were found to play a role in tropical tropopause cirrus formation [*Froyd et al.*, 2010], while metallic, crustal, and carbonaceous particles were identified as INPs in the upper troposphere and lower stratosphere [*Chen et al.*, 1998]. Soot and biomass burning particles were found to be a minor component in cirrus ice residuals [*Twohy and Poellot*, 2005; *Cziczo and Froyd*, 2014] but were found to be a considerable fraction (~27%) in mixed-phase clouds at the Jungfraujoch observatory (3571 m asl) in Switzerland [*Cozic et al.*, 2008]. While another study at the Jungfraujoch observatory found only a minor fraction (2%) of soot and soot associated with mineral dust in ice residues [*Kamphus et al.*, 2010], a more recent study also at the Jungfraujoch observatory, during winter time, found that long-range transported Saharan dust, mixtures of basaltic dust from bedrock, and marine aerosol (sea salt and a nonfluorescent organic) constitute a major fraction of INPs [*Boose et al.*, 2016]. These studies reveal that long-range transported particles in the free troposphere lead to a diversity of INP types.

Organic matter is ubiquitous in the atmosphere, accounting for 20–90% of the submicron aerosol mass in most environments [*Kanakidou et al.*, 2005]. However, the role of organic compounds and their phase state on heterogeneous ice nucleation is still poorly understood. Ice nucleation studies on particles generated in the laboratory and collected in the field found that organic, sulfate, or nitrate coating can inhibit or decrease the ice nucleation ability of particles. Other studies have demonstrated that organic particles can act as INPs, however, not as efficiently as mineral dust particles [*Kanji et al.*, 2008; *Möhler et al.*, 2008; *Knopf et al.*, 2010; *Murray et al.*, 2010; *Wagner et al.*, 2012; *Wang et al.*, 2012a, 2012b; *Wilson et al.*, 2012; *Baustian et al.*, 2013; *Knopf et al.*, 2014; *Schill et al.*, 2014; *Kulkarni et al.*, 2016]. It has been suggested that the presence of coating material decreases ice formation potential of dust particles, perhaps due to the reactive nature of the coating altering the INP surface and cloaking the ice nucleation active sites, or changing the water activity [*Möhler et al.*, 2008; *Cziczo et al.*, 2009; *Eastwood et al.*, 2009; *Sullivan et al.*, 2010; *Knopf and Alpert*, 2013; *Wex et al.*, 2014; *Kulkarni et al.*, 2015]. However, coating by biological substances such as some types of proteins and polysaccharides promotes ice nucleation [*Pummer et al.*, 2015]. A recent study investigated immersion freezing of dust collected from the ground [*Kaufmann et al.*, 2016b]. The study found that while mineral composition impacted freezing ability, it was insufficient to fully explain all of the data. The authors speculated that either mineral mixtures or dust aging, i.e., acquiring organic coatings, prevented extreme low or high freezing temperatures typically observed for purified or commercially available minerals. The presence of organic material further complicates prediction of ice nucleation because it can exhibit amorphous phase states including liquid, semisolid, and solid (glassy) phases, thereby, at certain thermodynamic conditions, providing solid surfaces that facilitate immersion freezing (IMF) and deposition ice nucleation (DIN) [*Murray et al.*, 2010; *Wang et al.*, 2012a; *Wilson et al.*, 2012; *Berkemeier et al.*, 2014; *Lienhard et al.*, 2015]. For example, glassy aerosol likely influences heterogeneous ice nucleation in tropical tropopause cirrus clouds [*Murray*, 2008; *Froyd et al.*, 2010]. Equilibrium time scales for water vapor uptake on laboratory-generated secondary organic aerosol (SOA) can vary significantly; upon an increase in *RH*, a glassy organic particle may act as immersion and deposition INP or it might transition to the liquid phase, the latter process inhibiting heterogeneous ice nucleation [*Wang et al.*, 2012a; *Berkemeier et al.*, 2014; *Lienhard et al.*, 2015]. In photochemically active environments, such as in a pollution plume, organic material typically dominates and coats aerosol particles, which act as DIN and IMF [*Knopf et al.*, 2010; *Wise et al.*, 2010; *Baustian et al.*, 2012; *Wang et al.*, 2012b; *Knopf et al.*, 2014], thus warranting further study on the role of aged ambient organic aerosol to form ice.

During long-range transport, particles experience aging processes including redistribution of organic compounds [*Kroll et al.*, 2009; *Dzepina et al.*, 2015] and hydrophilic material, chemical modification by reaction with oxidants such as O_3, OH, and NO_3 [*George and Abbatt*, 2010; *Knopf et al.*, 2011]; coagulation with other materials [*Chapleski et al.*, 2016]; and cloud cycling [*Hoose et al.*, 2008]. These processes may affect a particle's ability to act as an INP [*Cziczo et al.*, 2009; *Wang and Knopf*, 2011] by masking the original particle surface properties. The link between ice nucleation efficiency and particle chemical composition and modifications to the internal mixing state due to long-range transport remains largely unresolved, in part because of a lack of field data.

Here we discuss the heterogeneous ice nucleation activity in the DIN and IMF modes by aged particles that were collected at Pico Mountain Observatory (PMO) at 2225 m asl in the North Atlantic Ocean. The remote

Table 1. Sampling Date, Duration, Plume Age, Estimated Mass of Organic Matter, and Concentration and Size of the Particle Population and of the INPs[a]

Sample#	Sampling Date and Times (2013)	Plume Age (Day)	OC/EC	OM ($\mu g\, m^{-3}$)	D_{Aeq} (μm)	N_d ($\times 10^5\, mm^{-2}$)	A_s (mm^2)	f_A ($\times 10^{-6}$)	d_{INP} (μm)	N_{INP} (L^{-1})
SA1	23 Aug 20:50–22:18	11.6	65.8	1.73 (±0.13)	0.56 (±0.53)	3.0 (±3.3)	0.06 (±0.03)	4.2 (±1.7)	NA -	0.06 (±0.13)
SA2	27–28 Aug 19:55–14:15	12.3	36.4	0.97 (±0.16)	0.68 (±1.12)	5.4 (±1.8)	0.15 (±0.02)	4.0 (±0.5)	2.88 (±1.67)	0.03 (±0.20)
SA3	7–8 Sept 16:25–15:32	12.0	24.7	0.19 (±0.13)	0.61 (±0.90)	3.9 (±2.6)	0.23 (±0.06)	10.6 (±2.8)	3.85 (±1.68)	0.01 (±0.04)
SA4	19–20 Sept 16:48–14:00	17.3	6.5	0.02 (±0.14)	1.02 (±1.33)	1.2 (±1.8)	0.10 (±0.05)	14.4 (±8.2)	3.52 (±1.58)	0.01 (±0.01)

[a]Ratio of organic carbon and elemental carbon (OC/EC), estimated organic mass (OM), mean area equivalent diameter (D_{Aeq}), mean particle number density (N_d) on the substrate exposed during the ice nucleation experiments, and total surface area of the particles (A_s) available for ice nucleation, activated fraction (f_A), INP diameter (d_{INP}), and estimated number of INP (N_{INP}) per liter of air (average value from all the experiments) at 223 K. The numbers in parentheses for OM represent the measurement uncertainty, which includes the blank subtracted values. The numbers in parentheses for the other values represent the standard deviation for D_{Aeq}, N_d, and d_{INP}, and uncertainties for A_s, f_A, and N_{INP} are propagated from D_{Aeq} and N_d. For SA1, d_{INP} is not available (NA).

location of PMO allows access to free tropospheric particles that are transported over long distances [*China et al.*, 2015; *Dzepina et al.*, 2015]. We investigate four particle samples collected at PMO with different air mass ages and transport patterns. The particles were probed for their physicochemical characteristics and ability to heterogeneously nucleate ice. INPs were identified and characterized for morphological and elemental compositions using electron microscopy. The limited number of samples analyzed here provides a valuable but nonconclusive perspective on the general picture of the role that particles transported over long distances might have on ice formation, including an understanding of the effects of season and transport time. However, our analysis still allows us to demonstrate the importance of PMO as a unique remote free tropospheric sampling site for ice nucleation studies. In addition, our analysis provides preliminary evidence of how differently long-range transported particles behave in terms of ice formation, with respect to particles studied previously in the laboratory, near-field experiments, or simply for different environments, thus warranting further studies.

2. Experimental Methods

2.1. Sampling Site and Sample Collection

PMO is located in the summit caldera of Pico Mountain on Pico Island at 2225 m asl, in the Azores, Portugal (38.47°N, 28.40°W). PMO can be reached only by foot after a strenuous hike, starting at 1225 m asl. The observatory, located far from source emissions and typically above the marine boundary layer, receives air that has been transported for long distances over the North Atlantic Ocean [*Honrath et al.*, 2004; *Kleissl et al.*, 2007; *China et al.*, 2015; *Dzepina et al.*, 2015]. As part of a pilot study on ice nucleation, aerosol samples were collected at PMO during late summer of 2013 on silicon nitride-coated disks (3 mm diameter; PELCO®, Ted Pella, Inc.). The particles were collected on the second stage of a four-stage cascade impactor (MPS-4G1) with a 50% cutoff diameter of 0.50 μm. Particle concentrations were measured using a two-channel (>0.3 μm and >0.4 μm) laser particle counter (MetOne GT521). High-volume samplers (EcoTech HiVol 3000) were used to collect aerosol on quartz filters for chemical characterization. The off-line chemical analysis included organic carbon (OC) and elemental carbon (EC) contents, using an EC-OC analyzer (Sunset Laboratory Inc., Model 4), and quantification of common cations and anions, using an integrated ion chromatography (IC) system (Thermo Scientific ICS-1100/ICS-2100). We collected additional samples for electron microscopy analysis on nucleopore filters (100 nm pore, Whatman) and lacey formvar grids (300 mesh, Ted Pella, Inc.) using a custom-made sequential sampler [*China et al.*, 2015]. Table 1 reports the sampling times and conditions. Additional experimental details are provided in the supporting information.

2.2. Retroplume Analysis

In this study, we used the backward mode of the Lagrangian Flexible Particle (FLEXPART) dispersion model [*Seibert and Frank*, 2004; *Stohl et al.*, 2005; *Owen and Honrath*, 2009] to find the origin of sampled air masses and their transport trajectories to PMO. Every 3 h, 10,000 passive air parcels were released from PMO and transported backward in time and space up to 20 days, globally. FLEXPART calculated three-dimensional matrices of residence times of the air parcels in the output grid cells at the upwind time steps (every 3 h). The integration of the matrices over time and altitude provided an upwind spatial distribution of the particle residence times, also referred to as a "retroplume." This distribution shows the degree of dispersion and relative contributions from air masses of varying locations and altitudes. In order to estimate air mass ages
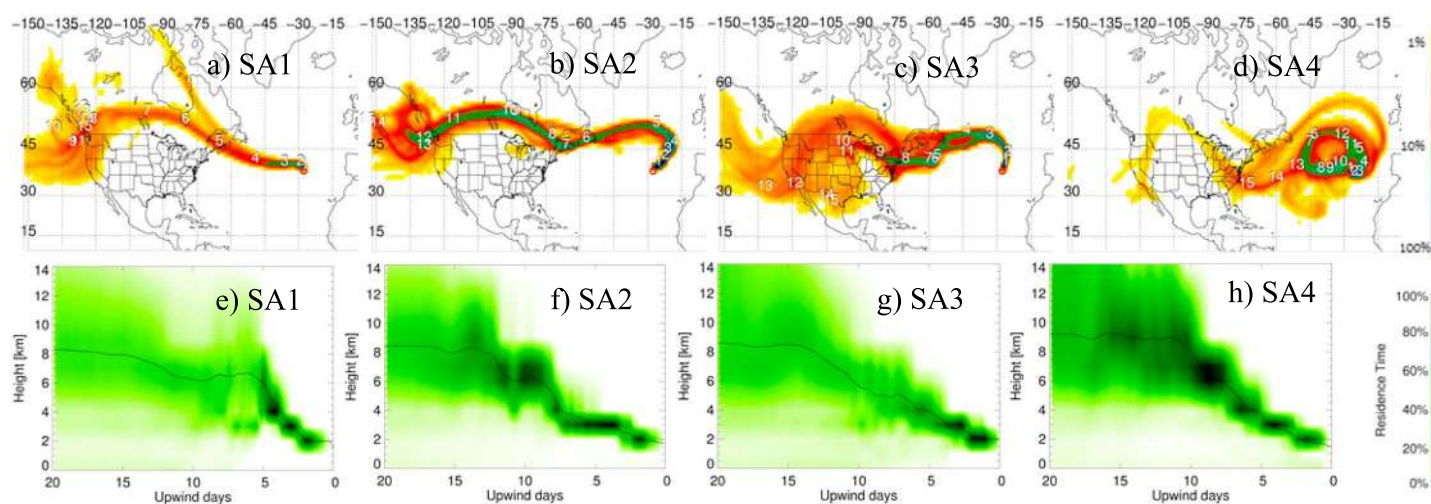
Figure 1. Representative FLEXPART retroplumes for the time periods of the samples collection. (top) Residence time integrated over the vertical column and over the 20 day transport time. The places of the white labels indicate the estimated locations of the center of the plume on the transport days (back in time from PMO). The abundance of residence time at each pixel is color coded by logarithmic grades representing its ratio to the location of maximal integrated residence time (100%). (bottom) Vertical distribution of retroplume residence time at given upwind times. The black line indicates the mean height of the plume during transport.

at PMO, we folded (i.e., multiplied) the retroplume with the concentrations of a pollution tracer (a sampling process as described in *Zhang et al.* [2014]), i.e., using the anthropogenic and wildfire CO emission inventories [*Olivier and Berdowski*, 2001; *Mu et al.*, 2011]. We estimated air mass ages by calculating the average time of CO being transported in FLEXPART.

Figure 1 shows the retroplumes for the particle collection periods. The top plots are column-integrated horizontal residence time distributions (from the surface to 15,000 m asl), and the bottom plots show the vertical distribution of the retroplume residence time for the 20 day transport period. The air masses that reached PMO during the collection period of sample SA1 were transported mostly from North America (especially Canada) and continuously mixed with boundary layer air for upwind days 10–20 (Figure 1b). Sample SA2 was also affected by North American air masses and possibly by marine air due to an early subsidence followed by residence for ~7 days at 2–3 km over the Atlantic Ocean (Figure 1f). The air masses corresponding to SA3 tracked over a wide area of the U.S. and Canada and mixed with boundary layer air through upwind days 7–20 (Figures 1c and 1g). During upwind days 4–7, SA3, the transported air mass may have interacted with marine boundary layer air. The air masses during SA4 were the most aged (~17.3 days) with air recirculation over the ocean. In Table 1, we report the average estimated plume age for each sample.

2.3. Ice Nucleation and Water Uptake Experiments

Ice nucleation and water uptake experiments were conducted using a vapor-controlled cryo-cooling stage consisting of an ice nucleation cell and an optical microscope [*Wang and Knopf*, 2011; *Knopf et al.*, 2014], similar to other optical microscope setups [*Baustian et al.*, 2012; *Wise et al.*, 2012; *Schill et al.*, 2014]. Substrates were placed inside the ice nucleation cell and exposed to humidified nitrogen gas (N_2, ultra-high purity) flowing at 1 standard liter per minute at a constant dew point temperature, T_d. The T_d was measured by a chilled mirror hygrometer (GE Sensing) at the outlet of the ice nucleation cell with an uncertainty of ±0.15 K. Once T_d was stable, RH with respect to ice, RH_{ice}, was increased by cooling the substrate at a rate of 0.1 K min^{-1} corresponding to an RH_{ice} increase of ~1.5–2.3% per minute, reflecting atmospheric conditions [*Kärcher and Ström*, 2003]. Particle temperature, T_p, and T_d values were used to calculate the RH_{ice} [*Murphy and Koop*, 2005].

Water uptake experiments were conducted using a magnification of 1130X while ice nucleation experiments were conducted at 230X. Optical images of the sample, T_d, and T_p were simultaneously recorded every 0.02 K. Optical images allowed us to identify the changes in particle phase and size during water uptake or ice nucleation of particles larger than 0.2 μm and 1 μm using a magnification 1130X and 230X, respectively [*Wang and Knopf*, 2011]. A freezing event was considered IMF if water uptake by a particle was observed

prior to the formation of ice, while it was considered DIN if no water uptake was observed before ice formation. DIN experiments were performed first at colder temperatures to avoid potential effects on particle morphology and chemical composition changes during water uptake experiments and IMF at higher temperatures. We recorded the initial RH_{ice} and T_p conditions, i.e., the conditions at which the first particle was observed to nucleate ice. We performed at least three experiments at each dew point. The sample was warmed to 275 K for 15 min between subsequent experiments to ensure complete sublimation of ice crystals and to avoid potential preactivation [*Knopf and Koop*, 2006]. After each ice nucleation event, a calibration experiment was conducted to calibrate T_p against T_d as described in *Wang and Knopf* [2011]. Experimental uncertainties were calculated from the uncertainties of $\Delta T_d < \pm 0.15$ K and $\Delta T_p < \pm 0.3$ K [*Wang and Knopf*, 2011].

During the ice nucleation experiments, the entire sample area was monitored at once. This procedure avoids missing the detection of INPs that may have nucleated at lower RH_{ice} and potential artifacts in the RH distribution due to ice forming outside the field of view. For each independent experiment, the ice nucleation onset observed was the first particle in that sample to nucleate ice. Only the first ice nucleation event was reported since the presence of ice could lead to changes in RH_{ice} above the particles at the low cooling rates used in these measurements. Although activation of all particles cannot be achieved by this method, the first ice formation event represents the precise thermodynamic conditions at which air containing a similar particle population would initiate ice crystal formation and, in addition, allows for the unambiguous identification of the ice nucleation process (IMF and DIN), deliquescence, or liquid-liquid phase separation [*Bertram et al.*, 2011; *Wise et al.*, 2012; *Schill and Tolbert*, 2013; *Schill and Tolbert*, 2014]. The optical microscope method intrinsically possesses high detection sensitivity, being able to determine activated fractions in the range of 10^{-6}. This method can be applied to derive ice nucleation parameters such as frozen fraction (*f*), active surface site densities (n_s), or heterogeneous ice nucleation rate coefficients (J_{het}) [*Dymarska et al.*, 2006; *Kanji and Abbatt*, 2006; *Kanji et al.*, 2008; *Knopf and Lopez*, 2009; *Knopf et al.*, 2010; *Alpert et al.*, 2011; *Knopf et al.*, 2011; *Murray et al.*, 2011; *Wang and Knopf*, 2011; *Broadley et al.*, 2012; *Wang et al.*, 2012a, 2012b; *Knopf and Alpert*, 2013]. A comparison of deposition ice nucleation, including J_{het} values due to the clay mineral kaolinite, is presented in Figure S5 in the supporting information, demonstrating the agreement of our technique [*Wang and Knopf*, 2011] with the continuous flow diffusion chamber technique [*Kanji et al.*, 2013]. Lastly, the microscopy approach is well suited to identify INPs and to scrutinize these particles in terms of chemical composition and morphology with subsequent comparison with non-INPs [*Baustian et al.*, 2012; *Hiranuma et al.*, 2013; *Knopf et al.*, 2014].

2.4. Single-Particle Analysis and Ice Nucleating Particle Identification

We analyzed single particles using a field emission scanning electron microscope (SEM) (Hitachi S-4700) on the same silicon nitride substrates, but only after having concluded the ice nucleation experiments, to avoid possible damage due to electron beam exposure. On numerous, randomly selected particles we conducted energy dispersive X-ray spectroscopy (EDS) to determine the elemental composition and the particle internal mixing state and to assess the chemical composition and morphology of the ambient particle population. Furthermore, individual INPs were identified from recorded optical microscopy images of ice nucleation experiments (as described in *Knopf et al.* [2014]) and were then relocated in the SEM for microscopic characterization. Figure 2 shows an example of INP identification from optical microscopy images and SEM. Lacey grids were examined using transmission electron microscopy (TEM) (JEOL JEM-2010) to further investigate the individual particle morphology and internal mixing state.

3. Results and Discussions

3.1. Particle Characterization

The average particle number concentrations ($>0.3 \, \mu m$ in diameter) measured by the optical particle counter were 13.2, 6.6, 1.1, and 0.4 cm^{-3} for SA1, SA2, SA3, and SA4, respectively. The mean particle 2-D projected area equivalent diameter, D_{Aeq}, ranged from 0.56 (SA1) to 1.02 μm (SA4) (Figure S1 and Table S1 in the supporting information). We note that the projected geometric diameter (D_{Aeq}) obtained from 2-D SEM images may differ from the aerodynamic diameter given by the impactor and the optical diameter classification provided by the optical particle counter. The particle number density (N_d) and the total number of particles available for ice nucleation on the substrate were estimated directly from the SEM images.
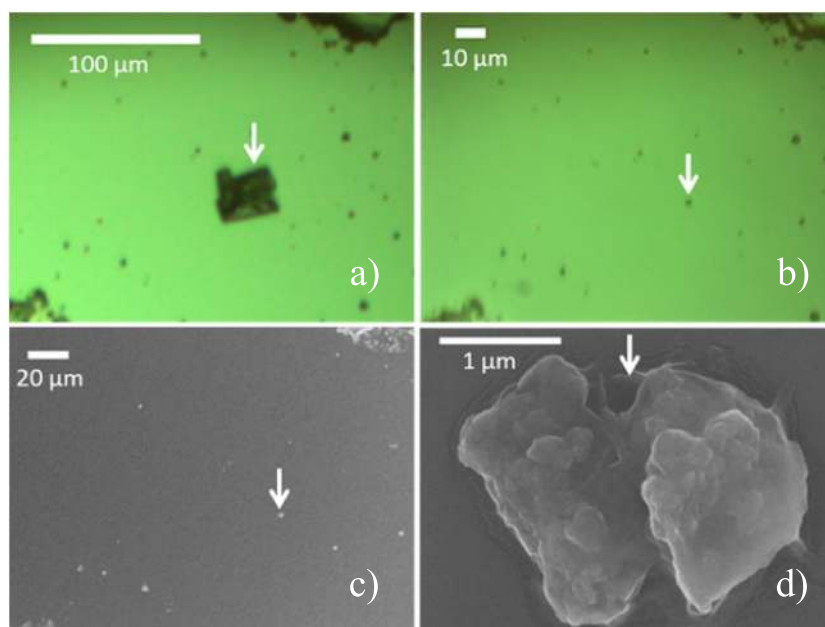
Figure 2. Example of ice nucleating particle (INP) identification from optical microscope images and SEM for SA4. (a) An ice crystal initiated by an INP (white arrow) and (b) the same after sublimation. (c) SEM image of the same field of view and (d) magnified view.

The total particle surface area on the substrate for ice nucleation was calculated from D_{Aeq}, N_d, and the sample area observed. The sample area for the ice nucleation experiments is $0.8\,mm^2$. Uncertainties for the total surface area of the particles were propagated from D_{Aeq} and N_d. The mean values and uncertainties are reported in Table 1. The value of N_s ranges from 0.06 (SA1) to 0.23 (SA3) mm^2.

Figure 3 shows some representative TEM images of particles examined in this study. TEM images show that mineral dust, soot, sulfate, and other material are internally mixed and coated by organic matter. Soot and organic matter are identified in the TEM from their morphological properties; soot particles have graphitic layers, while organic matter has disordered, amorphous structures. Often atmospheric particles are engulfed within coating material and classified as embedded particles [*Adachi and Buseck*, 2008; *China et al.*, 2013]. A major fraction (~50–65%) of the particles in our PMO samples is embedded within organic matter for all four samples. The type of organic coating on individual particles can be different and can have different origins. Organic coating can be acquired at the source during emission or during the long-range transport. However, the identification of different types of organic coating is not feasible with the data available from this study. Additional SEM images are shown in Figure S2. Most of the particles in all four samples are mixtures of soot (C and O); mineral dust (Al, Ca, and Fe); fresh (Na, Cl, and Mg); and aged (Na, Mg, and S, with depleted Cl) sea salt, sulfate, and organic matter, as identified by EDS analysis. SA1 is dominated by smaller particles ($<0.4\,\mu m$), mostly coated soot with a minor contribution of mineral dust particles. IC data from bulk aerosol analysis show that oxalate, malonate, and succinate are elevated in SA1, suggesting an aged anthropogenic pollution influence [*Song and Gao*, 2009]. SA2 is dominated by fresh and aged salt particles and by mineral dust mixed with salt. In SA3, most particles are internally mixed with mineral dust, salt, soot, and sulfate. SA4 is dominated by dust and soot particles, while internally mixed soot and dust particles represent a lower fraction than in SA3. Sulfate and nitrate are also abundant in all four samples among the anions, with the maximum concentration of nitrate in SA2 and the maximum concentration of sulfate in SA1 (Table S2 and Figure S3). The mean OC/EC ratio ranges between 6.5 and 65.8 (Table 1). From the OC concentration, we estimated the organic mass (OM) assuming an OM:OC ratio of 1.8 [*Pitchford et al.*, 2007] representative of remote locations. Organic mass ranges from $0.02\,\mu g\,m^{-3}$ to $1.73\,\mu g\,m^{-3}$ with the highest concentration during SA1 and the lowest concentration during SA4. A previous study at PMO showed that organic compounds often comprise the largest fraction ($57 \pm 21\%$) of the total aerosol mass [*Dzepina et al.*, 2015].
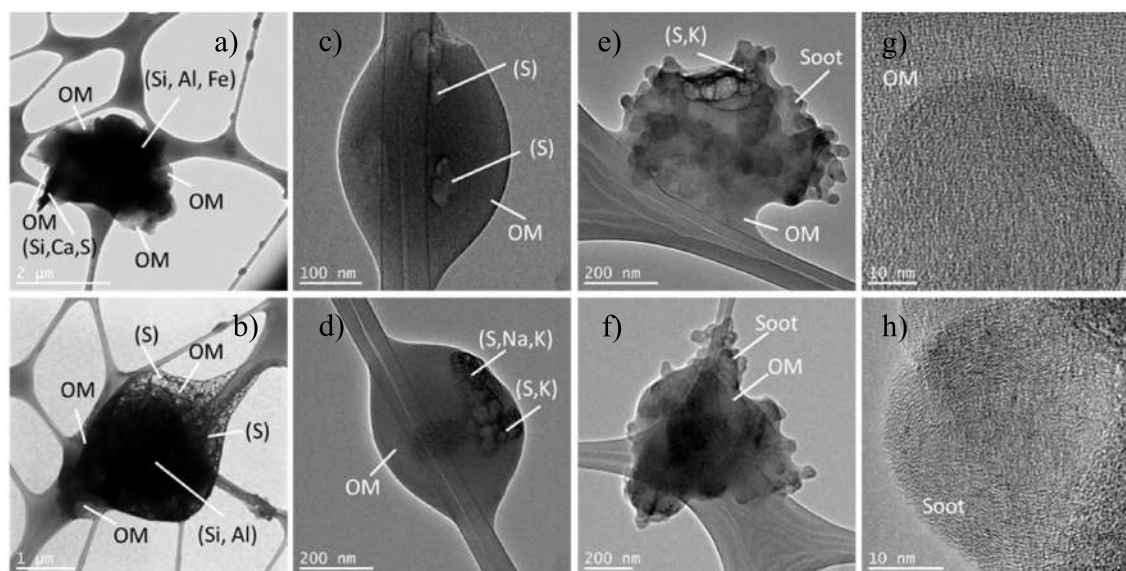
Figure 3. TEM images representative of the particle population: (a and b) coated dust, (c and d) coated sulfate particle, and (e and f) coated soot. High-resolution TEM images of (g) organic matter (OM) with amorphous structure and (h) soot particle with graphitic layers. Elemental compositions of particles were obtained using EDS and are given in parentheses. C and O were present in each particle but are not shown here.

3.2. Water Uptake and Ice Nucleation

The mean conditions for initial DIN and IMF events and water uptake are shown as a function of T_p and RH_{ice} in Figure 4a, and Figure S4 shows additional examples of water uptake experiments. Water uptake occurred on most of the particles, but not on all of them. Water uptake occurred from 44% to 66% RH between 238 K and 267 K; however, some sample consistently required less or more humid conditions than others before condensed water was observed. For example, sample SA2 took up water at the lowest RH values in the range of 42–47% compared to other samples, suggesting that particles on SA2 are more hygroscopic. For SA1, which is dominated by coated soot, water uptake occurred between 57 and 61% RH. SA3 and SA4 took up water between 49–60% and 49–66% RH, respectively, even though the particles contain sea salt, known to be highly hygroscopic. We emphasize that the samples collected at PMO are complex mixtures of sea salt, dust, and soot particles coated by sulfate and organic material. Due to the presence of organic acids (e.g., oxalate, malonate, and succinate), sulfate and nitrate, one would expect that low RH is required for water uptake (Figure S3). Multicomponent mixtures of organic acids and salt have been previously shown to deliquesce at RH as low as 27% [*Marcolli et al.*, 2004], which may also explain the low RH water uptake observed here. We suggest that despite the different origins of the particles and the initial chemical compositions, mixing and chemical aging during long-range transport alter their ability to take up water.

Ice nucleation occurred via IMF at 238 K and 248 K near or below water saturation between 90 and 100% RH (Figure 4a). Water uptake was observed at $T = 262–267$ K, but no subsequent ice formation occurred for any sample. IMF did not occur immediately after water uptake; instead, more dilute aqueous solutions were required to initiate IMF, which may explain why a narrow range of RH_{ice} for IMF was observed. Furthermore, using an aerosol thermodynamic model [*Friese and Ebel*, 2010], ionic concentrations are estimated in an aqueous solution considering only the presence of nitrate and sulfate at subsaturated conditions. Since ice formation occurred primarily between 90 and 100% RH, ionic concentrations are calculated ($wt_{NO3} = 9.3\%$, $wt_{SO4} = 5.4–4.7\%$, and $wt_{HSO4} = 2.2–2.9\%$, with total ionic concentration of $wt = 15.4\%$) at 90% RH as a limit for aqueous solution concentration. These results suggest that ice must have formed heterogeneously in the presence of aqueous solutions at $T = 235–245$ K (see supporting information).

At ~223 K, particles from all samples nucleated ice via the DIN at RH_{ice} between 112% and 128%, considerably lower than water saturation and the homogeneous freezing limit [*Koop et al.*, 2000]. Overall, the mean onset RH_{ice} varied only by 5% between samples. The green shaded area in Figure 4a indicates the range of
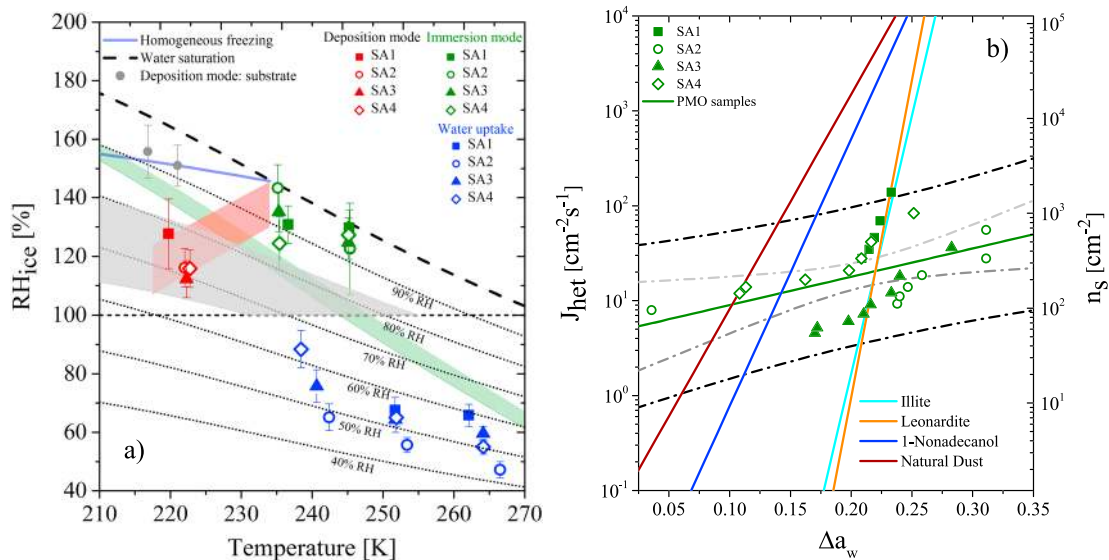
Figure 4. (left) Mean onset conditions for ice nucleation and water uptake. The solid blue line indicates the homogeneous freezing limit for $J_{hom} = 10^{10}$ cm^{-3} s^{-1} and $\Delta a_w = 0.313$ [*Koop et al.*, 2000; *Koop and Zobrist*, 2009]. The error bars are the standard deviations of the observed RH_{ice} or experimental uncertainties, whichever are larger. The gray symbols indicate the onsets of ice nucleation on a blank substrate. The red shaded area indicates the bounds of continental cirrus formation [*Heymsfield and Miloshevich*, 1995]. The gray shaded area indicates the estimated conditions required for ice nucleation in pores of sizes of 7.5–15 nm [*Marcolli*, 2014]. The green shaded area indicates the range of predicted glass transition temperature for laboratory-generated secondary organic aerosol [*Wang et al.*, 2012a]. (right) Experimentally derived heterogeneous ice nucleation rate coefficients, J_{het}, and active surface site densities, n_s (green symbols; note the different scale in the secondary y axis), as a function of Δa_w and J_{het} parameterizations for particle types illite (standard mineral dust), leonardite (standard humic acid), 1-nonadecanol [*Knopf and Alpert*, 2013], and natural dusts [*Niemand et al.*, 2012; *Alpert and Knopf*, 2016]. The solid green line is a log linear fit; the dotted gray and black lines along are the confidence and prediction bands at 95%, respectively.

predicted glass transition temperatures for laboratory-generated SOA [*Wang et al.*, 2012a], and Figure S6 discusses glass transition temperatures for different organic to sulfate ratios.

It has been hypothesized that DIN may occur through condensation of water and subsequent homogeneous freezing in pores [*Marcolli*, 2014]. DIN onsets at 223 K are within the range of condensation freezing in 7.5–15.0 nm pores, while surface features of ~5–40 nm were measured in coated INPs at PMO (Figure S7). Photochemically aged particles collected from the urban, polluted environment of Los Angeles nucleated ice in the DIN mode for RH_{ice}~138% [*Wang et al.*, 2012b], substantially less efficiently than the atmospherically aged particles from PMO for similar T_p and N_s (Table S3), while both the samples contain organic matter. Finally, we note that PMO samples had slightly different average surface areas (N_s of 0.06, 0.15, 0.23, and 0.10 mm^2 for samples SA1, SA2, SA3, and SA4, respectively), which may also explain the range of observed onset conditions [*Kanji et al.*, 2008; *Knopf and Alpert*, 2013].

Heterogeneous ice nucleation rate coefficients (J_{het}) are calculated as a function of the water activity criterion (Δa_w) [*Knopf and Alpert*, 2013]. The parameter Δa_w is a function of T and RH and is calculated by subtracting the a_w of the particles from the water activity point that falls on the ice melting curve at the same temperature [*Koop and Zobrist*, 2009]. As the experiment progressed in time, Δa_w increased from $\Delta a_w = 0$ at $RH_{ice} = 100\%$ until freezing was observed. Recent modeling results show that during and after a humidity-induced phase transition from solid to liquid-like, the aqueous solution associated with that particle readily equilibrates with its humidified environment under the applied experimental conditions [*Berkemeier et al.*, 2014]; therefore, we make the reasonable assumption that particle a_w is equal to relative humidity. Homogeneous freezing of pure water and micrometer-sized droplets of aqueous solution occurs at about $\Delta a_w = 0.313$ (Figure 4a), representing an upper limit for heterogeneous ice nucleation. Therefore, ice formation observed between $0 < \Delta a_w < 0.313$ is considered heterogeneous freezing. Particles exposed to water vapor during our experiments are assumed to be in equilibrium with their humidified environment, and thus, the a_w of the particles was set equal to RH. To derive J_{het} (Δa_w), the onset conditions of T and RH_{ice} from the experiments were used to calculate a_w and finally Δa_w. Then, discrete Δa_w intervals are defined by calculating Δa_w between $t = 12$ s time intervals, identical to the time between subsequent optical images used to

monitor ice nucleation [*Wang and Knopf*, 2011]. We note that due to the relationship between T, RH_{ice}, and Δa_w, consecutive Δa_w intervals are not the same. Repeated cooling cycles at similar T and RH_{ice} trajectories were conducted, and each is considered an independent ice nucleation experiment. Therefore, repeated experiments in which one freezing event was observed (the first freezing event) at the same conditions are equivalent to a single experiment that can monitor multiple freezing events. This allows derivation of J_{het} as a function of Δa_w following the equation, $J_{het} = N_{ice}/(t \cdot N_{s,tot})$. In any given interval of Δa_w, N_{ice} is the number of observed ice nucleation events that occurred. In other words, if one ice nucleation event occurred within a Δa_w interval, then $N_{ice} = 1$ for that interval. If two different experiments nucleated ice for the same value of Δa_w, then $N_{ice} = 2$ for that corresponding Δa_w interval. The total surface area, $N_{s,tot}$, is the sum of the particle surface area on the sample that nucleated ice in the specific Δa_w interval and the particle surface area for all other experiments that observed ice nucleation at a larger Δa_w. In other words, at a single ith interval, $\Delta a_w{}^i$, $N_{s,tot}{}^i$ accounts for all surface area available from experiments which nucleated ice between $\Delta a_w{}^i$ and $\Delta a_w{}^{i+1}$ and those experiments that detected ice formation at larger intervals or greater values of Δa_w. Ice active surface site densities, n_s, as a function of Δa_w, are also shown and calculated similarly, $n_s = N_{ice}/N_{s,tot}$.

Figure 4b shows J_{het} derived from the freezing data along with four parameterizations of different laboratory-investigated particle types, including (i) illite (standard mineral dust); (ii) leonardite (standard humic acid); (iii) 1-nonadecanol monolayer coatings; and (iv) natural Asian, Saharan, Canary Island, and Israel dusts [*Niemand et al.*, 2012; *Knopf and Alpert*, 2013; *Alpert and Knopf*, 2016]. Uncertainties in calculating J_{het} can stem from a variety of experimental errors or limitations, including uncertainties in the number of observed ice nucleation events, temperature, RH, and surface area. Following *Alpert and Knopf* [2016], we estimate a factor error in J_{het}, referred to as ΔJ_{het}, for the J_{het} parameterization given in Figure 4b (green curve). Here we quantified ΔJ_{het} in the form of a $\overset{\times}{\div}$ error (representing a factor error) because J_{het} varies exponentially over a linear range in T. Considering that we observed about 40 ice nucleation events $\left(\Delta J_{het} = \overset{\times 11}{\div 4}\right)$, a temperature uncertainty of ± 0.3 K $\left(\Delta J_{het} = \overset{\times}{\div} 2\right)$, an RH uncertainty of about $\pm 3\%$ $\left(\Delta J_{het} = \overset{\times}{\div} 10^{0.03 m} = \overset{\times}{\div} 1.2\right)$, and an error in surface area of about 1.5 orders of magnitude or a factor of about 32 $\left(\Delta J_{het} = \overset{\times 32}{\div 32}\right)$, results in a total J_{het} uncertainty of about a factor of 50 in the positive and 40 in the negative direction ($+1.7$ and -1.6 orders of magnitude). This parameterization uncertainty covers the J_{het} data scatter from all samples measured here and is greater than 95% prediction bands from the log linear fit (Figure 4b). We note that the slope of J_{het} versus Δa_w of the PMO samples changes by about 2 orders of magnitude in the investigated range and is much shallower compared with previous parameterizations of laboratory-generated and natural dusts. As previously stated, the collected particles are chemically complex and internally mixed with several inorganic elements and organic matter (Figure 3). Despite the fact that most of the samples contained mineral elements, J_{het} values for these limited PMO samples do not resemble parameterizations of laboratory freezing data for illite and natural dusts. Leonardite is a humic-like substance and may serve as a surrogate for the organic-rich particles observed at PMO. Parameterizations of immersion freezing due to leonardite, however, also do not match well with the observed freezing presented here. However, we note that the estimated J_{het} values for PMO samples represent an average over all kinds of particles with different sizes and types, rather than specifically for a single-particle type. Furthermore, J_{het} estimates are based on limited data and more experiments on multiple samples from various events are required to draw any firm conclusion. These preliminary results clearly warrant further investigation of the ice nucleating ability of long-range transported particles. We speculate that physicochemical transformations of the particles due to aging during the long-range transport can substantially impact their ice nucleation abilities. It is also possible that other minerals, organics and surfactants, not considered here, may be responsible for nucleating ice. Following the a_w-based IMF model [*Knopf and Alpert*, 2013], we provide a new J_{het} parameterization applicable specifically to the free tropospheric particles collected at PMO during this study and presented in Figure 4b, where $J_{het} = 10^{(m \times \Delta a_w + b)}$, $m = 2.981$, and $b = 0.656$ and $n_s = 10^{(m \times \Delta a_w + b)}$, $m = 2.981$, and $b = 1.735$. This new parameterization can assist in predicting IMF from free tropospheric aerosol over the Atlantic Ocean leading to ice cloud formation. Nevertheless, more experimental data are required to develop an improved parameterization that can be generalized for the remote free troposphere.

To simulate cloud processing, we repeated ice nucleation experiments in identical thermodynamic conditions by cycling particles through warm and cold temperatures as well as dry and humid conditions.
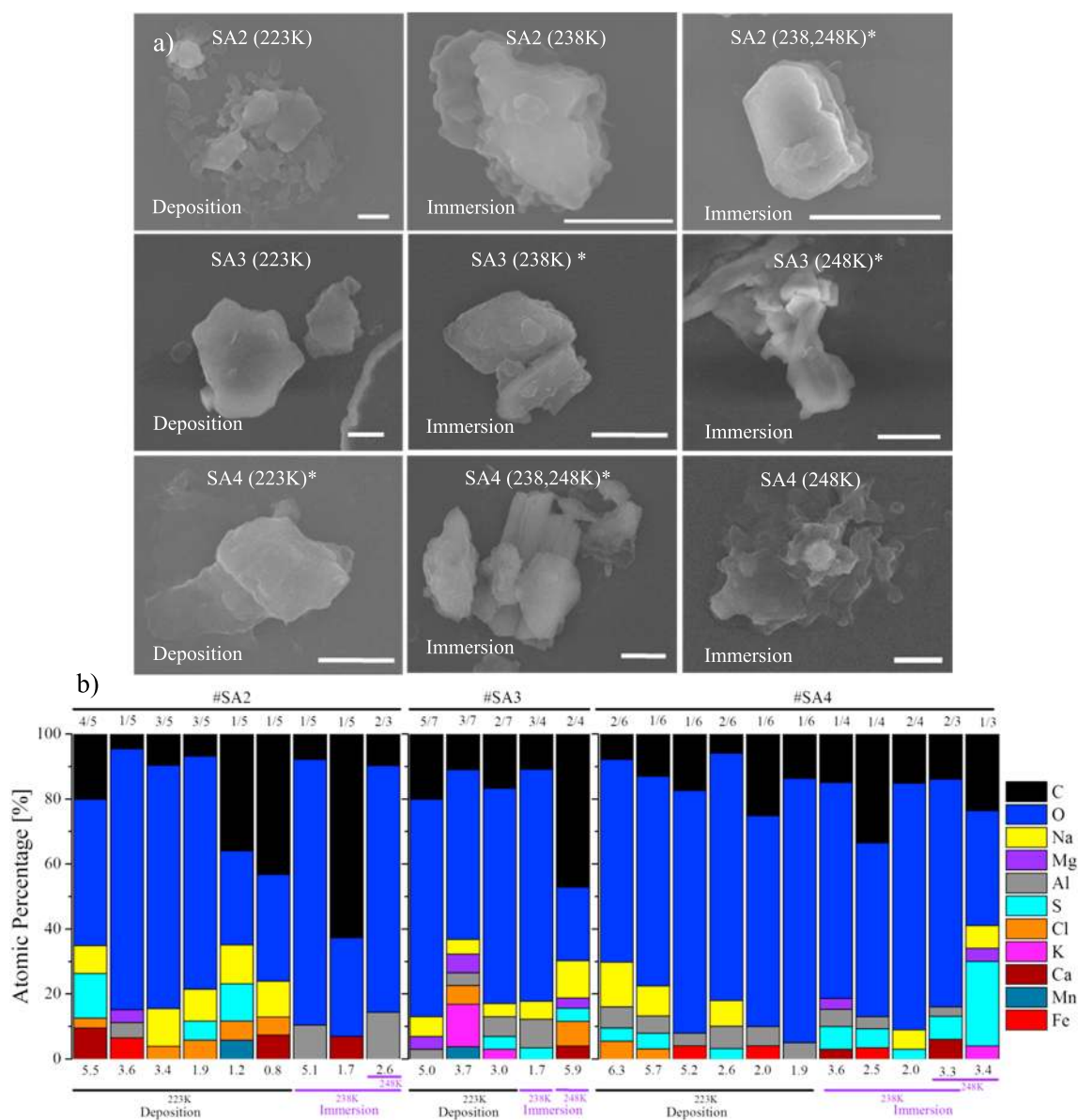
Figure 5. (a, top) Examples of identified INPs. The asterisk indicates INP that nucleated more than once. The scale bar is 1 μm. (b) Elemental composition for 25 identified INPs as a function of size (D_{Aeq} (μm), given below each bar) and ice nucleation mode and temperatures. The numbers at the top represent the frequency (number of times nucleated/total nucleation events) at which the same INP nucleated. The ordinate axis shows the relative abundance of atomic elements in percent after background subtraction. Si and N elements were not included in this analysis because of the background due to the silicon nitride substrate. Only distinct peaks (>3 atomic %) were used for this semiquantitative analysis.

Figure 5b reports the ice formation frequency of specific INPs (identified using SEM) at different temperatures. Thirteen out of the 25 identified particles nucleated more than once (Figure S8). *Wang et al.* [2012a] instead reported that DIN occurred on different particles, most of the time. In our study, some particles nucleated multiple times at two different temperatures (238 K and 248 K) via IMF. Although, not a single particle that nucleated at 223 K by DIN nucleated by IMF at either 238 K or 248 K. The average frequency (number of times nucleated/total nucleation events) is similar for both DIN (0.36) and IMF (0.43). It is not clear why some of the PMO particles formed ice multiple times. Because most INPs were coated, it is possible that once the particle initiated ice, the crystallization process restructured the particle surface [*Adler et al.*, 2013] influencing subsequent experiments. In a recent study, *Kaufmann et al.* [2016a] also observed that some macromolecules, from washing water samples of birch pollen, nucleated multiple times, while others did not.

Estimates of activated INP (N_{INP}) per liter of air via DIN mode at 223 K are given in Table 1. We note that these estimates are INP concentrations for given T and RH_{ice}. N_{INP} values were calculated from the observed INP-activated fraction (Table 1) and the total particle number concentration in air (ambient condition) measured by the optical particle counter ($>0.3\,\mu m$) during each sample collection. Observed activated fractions are calculated using the ratio of the number of ice crystals formed simultaneously to the total number of particles on the substrate. This calculation yields N_{INP} of 0.06 ($\pm$0.13), 0.03 ($\pm$0.20), 0.01 ($\pm$0.04), and 0.01 ($\pm$0.01) L^{-1} for samples SA1, SA2, SA3, and SA4, respectively, at 223 K. Note that N_{INP} values have large uncertainties, originating from the uncertainties associated with the total particle surface area and the particle number density on the substrate. N_{INP} values and their uncertainties are reported in Table 1. These estimated N_{INP} values provide a lower limit since the total particle concentration may be underestimated due to the fact that we used the total particle concentration measured by the optical particle counter that counts only particles larger than 0.3 μm.

Concentrations of INPs measured in the free troposphere can be compared with the results presented here. N_{INP} can be calculated from Figure 4b using available atmospheric and aerosol parameters, T, RH, and S_{tot}, where S_{tot} is the total particle surface area per volume of air. S_{tot} was estimated using the particle concentration data from the optical particle counter and the particle surface area measurements from the SEM images, yielding an uncertainty of 1.5 orders of magnitude. When assuming a time-dependent freezing process, $N_{INP} = J_{het} \times S_{tot} \times t$, where t is the time for ice nucleation to occur. Ice nucleation examination times for many field-deployed instrumentation is on the order of 10 s [e.g., *DeMott et al.*, 2003; *Chou et al.*, 2011]. For PMO, the derived J_{het} values from experimental data range between 5 and 140 $cm^{-2}\,s^{-1}$ for $\Delta a_w = 0.04-0.31$, respectively (Figure 4b) and mean $S_{tot} = 2.4 \times 10^{-5}\,cm^2\,L^{-1}$. Employing $t = 10$ s results in $N_{INP} = 0.0012-0.03\,L^{-1}$. Allowing for 20 min of ice particle production in a cloud, i.e., $t = 1200$ s, $N_{INP} = 0.14-4.0\,L^{-1}$. It is worthwhile noting that the INP concentrations calculated here can be lower than the typical instrument detection limit of instruments employed in field experiments such as the continuous flow diffusion chamber (CFDC), for which the typical detection limit is above 0.1 INP L^{-1} [*DeMott et al.*, 2010; *DeMott et al.*, 2016], although it can be below 0.1 INP L^{-1} when using an aerosol concentrator [*Tobo et al.*, 2013]. For example, at the free tropospheric station, Jungfraujoch in Switzerland, INP concentrations at $\Delta a_w = 0.20$ (i.e., $RH = 0.93$, $T = 241$) were about 1.0 L^{-1}, although measurements were frequently below instrument detection, which ranged between 0.1 and 1 L^{-1} [*Boose et al.*, 2016]. We provided an estimation of INP concentration (Figure S9) to compare with mixed-phase cloud conditions and existing published measurements, typically conducted at water saturation ($RH = 100\%$ or $a_w = 1.0$). Figure S10 provides a comparison of the INP concentration for several field measurements as a function of temperature, for $a_w = 1.0$ and ice nucleation times $t = 10$ s, 1 min, and 20 min. We note that this comparison depends on the assumption that ice nucleation on ambient particles will continue as a function of time when all other conditions and variables are constant. We also draw attention to the uncertainties in this calculation, which are about $\pm 1-2$ orders of magnitude in J_{het} [*Knopf and Alpert*, 2013; *Alpert and Knopf*, 2016] and ± 2 orders of magnitude representing the range of S_{tot}. Predictions of N_{INP} may provide a benchmark in this low INP concentration range. In other words, when increasing RH at a given T, N_{INP} derived from our method should converge with the lower bound of CFDC measurements as exemplified in Figure S10.

3.3. Identification of Ice Nucleating Particles

We were able to identify a total of 25 individual INPs from 3 of the 4 samples (9 from SA2, 5 from SA3, and 11 from SA4). Examples of INPs observed in SA2, SA3, and SA4 at different temperatures and freezing modes are displayed in Figure 5a. The D_{Aeq} of the INPs ranges between 0.84 and 6.32 μm with a mean of 3.35 μm. Each INP is associated with O and C, O being the most abundant. Other common elements are Na, S, Al, Ca, K, Cl, Mg, and Fe (Table S4). Elemental composition, represented as atomic percent, is shown in Figure 5b as a function of particle size, freezing mode, and temperature. Similarly to a previous study [*Knopf et al.*, 2014], we find no clear trends in INP composition with regard to ice nucleation modes, freezing temperatures, and particle size. We note that all INPs and non-INPs are associated with C- and O-rich material.

As mentioned above, the TEM analysis of particle population demonstrates the predominance of coated particles (Figure 3). In general, the DIN RH_{ice} values for samples SA2, SA3, and SA4 are remarkably similar

despite the different air masses and particle types. We hypothesize that at cold temperature, the outer organic coating may control the ice nucleation even if the core of the particle is dust, sulfate, or sea salt [*Knopf et al.*, 2010]. It is possible that organic coatings or organic particles transitioned to a glassy state at 223 K [*Berkemeier et al.*, 2014], as discussed in the supporting information and Figure S6. This may be evident from the apparent discontinuity in RH onsets between IMF and DIN occurring at 88–100% and 70–78%, respectively. All the DIN events were observed below the predicted range of glass transition temperature (T_g) of anthropogenic derived SOA material (Figure 4a), although the presence of sulfate can affect T_g [*Koop et al.*, 2011] (Figure S6). We hypothesize that glass formation of the organic material present on particles might explain why DIN occurred in a narrow RH_{ice} range, even when the overall composition varied significantly among particles and samples. We speculate that a reason for the slight variability in the onset RH_{ice} between samples (between 112% and 128% and mean onset at a given T varies by 5% between samples) for DIN could be the thickness of the coating on the particles, because thin coating may only partially mask the surface of the particle included within [*Kanji et al.*, 2008; *Möhler et al.*, 2008; *Wise et al.*, 2010; *Wang et al.*, 2012b; *Chou et al.*, 2013]. More studies investigating the effect of glassy organic coatings on ice nucleation are needed to further our understanding of these processes.

4. Conclusions

In this study, we report unique observations of ice nucleation and water uptake of aged free tropospheric particles collected at PMO. The data suggest that typically aged, free tropospheric particles at PMO promote ice formation by immersion freezing and deposition ice nucleation. Most identified INPs are internally mixed with organic and inorganic materials. Bare particles, such as pure soot or mineral dust, are absent, indicating that either organic coatings were acquired close to their source in photochemically active regions or that even under free tropospheric conditions, secondary organic material condensed onto accumulation mode particles and INPs. Glassy organic coatings on particles at low temperatures may be responsible for the remarkably similar ice formation conditions, despite different particle sources and types, suggesting that the internal mixing state of individual particles plays a critical role in ice nucleation. Our results demonstrate that free tropospheric particles collected at PMO, which experience physical and chemical aging while being transported across the Atlantic Ocean, can participate in cloud glaciation processes by immersion freezing and deposition ice nucleation, potentially impacting mixed-phase and cirrus cloud formation and thus the regional hydrological cycle, radiative transfer, and climate. Finally, we should caution that the results from this study are based on a limited number of samples collected over a 1 month period and that future studies should focus on analyzing larger sets of samples collected over longer periods and during different events and transport patterns to achieve more general insights on the ice nucleation characteristics of long-range transported, aged, and free tropospheric particles.

References

Adachi, K., and P. Buseck (2008), Internally mixed soot, sulfates, and organic matter in aerosol particles from Mexico City, *Atmos. Chem. Phys.*, 8(21), 6469–6481.

Adler, G., T. Koop, C. Haspel, I. Taraniuk, T. Moise, I. Koren, R. H. Heiblum, and Y. Rudich (2013), Formation of highly porous aerosol particles by atmospheric freeze-drying in ice clouds, *Proc. Natl. Acad. Sci. U.S.A.*, 110(51), 20,414–20,419, doi:10.1073/pnas.1317209110.

Alpert, P. A., and D. A. Knopf (2016), Analysis of isothermal and cooling-rate-dependent immersion freezing by a unifying stochastic ice nucleation model, *Atmos. Chem. Phys.*, 16(4), 2083–2107, doi:10.5194/acp-16-2083-2016.

Alpert, P. A., J. Y. Aller, and D. A. Knopf (2011), Ice nucleation from aqueous NaCl droplets with and without marine diatoms, *Atmos. Chem. Phys.*, 11(12), 5539–5555.

Avramov, A., and J. Y. Harrington (2010), Influence of parameterized ice habit on simulated mixed phase Arctic clouds, *J. Geophys. Res.*, 115, D03205, doi:10.1029/2009JD012108.

Baustian, K. J., D. J. Cziczo, M. E. Wise, K. A. Pratt, G. Kulkarni, A. G. Hallar, and M. A. Tolbert (2012), Importance of aerosol composition, mixing state, and morphology for heterogeneous ice nucleation: A combined field and laboratory approach, *J. Geophys. Res.*, 117, D06217, doi:10.1029/2011JD016784.

Baustian, K. J., M. E. Wise, E. J. Jensen, G. P. Schill, M. A. Freedman, and M. A. Tolbert (2013), State transformations and ice nucleation in amorphous (semi-)solid organic aerosol, *Atmos. Chem. Phys.*, 13(11), 5615–5628, doi:10.5194/acp-13-5615-2013.

Berkemeier, T., M. Shiraiwa, U. Pöschl, and T. Koop (2014), Competition between water uptake and ice nucleation by glassy organic aerosol particles, *Atmos. Chem. Phys.*, 14(22), 12,513–12,531.

Bertram, A., S. Martin, S. Hanna, M. Smith, A. Bodsworth, Q. Chen, M. Kuwata, A. Liu, Y. You, and S. Zorn (2011), Predicting the relative humidities of liquid-liquid phase separation, efflorescence, and deliquescence of mixed particles of ammonium sulfate, organic material, and water using the organic-to-sulfate mass ratio of the particle and the oxygen-to-carbon elemental ratio of the organic component, *Atmos. Chem. Phys.*, 11(21), 10,995–11,006.

Boose, Y., Z. A. Kanji, M. Kohn, B. Sierau, A. Zipori, I. Crawford, G. Lloyd, N. Bukowiecki, E. Herrmann, and P. Kupiszewski (2016), Ice nucleating particle measurements at 241 K during winter months at 3580 m MSL in the Swiss Alps, *J. Atmos. Sci.*, *73*(5), 2203–2228.

Broadley, S. L., B. J. Murray, R. J. Herbert, J. D. Atkinson, S. Dobbie, T. L. Malkin, E. Condliffe, and L. Neve (2012), Immersion mode heterogeneous ice nucleation by an illite rich powder representative of atmospheric mineral dust, *Atmos. Chem. Phys.*, *12*(1), 287–307, doi:10.5194/acp-12-287-2012.

Cantrell, W., and A. Heymsfield (2005), Production of ice in tropospheric clouds—A review, *Bull. Am. Meteorol. Soc.*, *86*(6), 795–807, doi:10.1175/BAMS-86-6-795.

Chapleski, R. C., Y. Zhang, D. Troya, and J. R. Morris (2016), Heterogeneous chemistry and reaction dynamics of the atmospheric oxidants, O_3, NO_3, and OH, on organic surfaces, *Chem. Soc. Rev.*, *45*, 3731–3746, doi:10.1039/C5CS00375J.

Chen, Y., S. M. Kreidenweis, L. M. McInnes, D. C. Rogers, and P. J. DeMott (1998), Single particle analyses of ice nucleating aerosols in the upper troposphere and lower stratosphere, *Geophys. Res. Lett.*, *25*(9), 1391–1394, doi:10.1029/97GL03261.

China, S., C. Mazzoleni, K. Gorkowski, A. C. Aiken, and M. K. Dubey (2013), Morphology and mixing state of individual freshly emitted wildfire carbonaceous particles, *Nat. Commun.*, *4*, 2122, doi:10.1038/ncomms3122.

China, S., et al. (2015), Morphology and mixing state of aged soot particles at a remote marine free troposphere site: Implications for optical properties, *Geophy. Res. Lett.*, *42*, 1243–1250, doi:10.1002/2014GL062404.

Chou, C., O. Stetzer, E. Weingartner, Z. Jurányi, Z. A. Kanji, and U. Lohmann (2011), Ice nuclei properties within a Saharan dust event at the Jungfraujoch in the Swiss Alps, *Atmos. Chem. Phys.*, *11*(10), 4725–4738, doi:10.5194/acp-11-4725-2011.

Chou, C., Z. A. Kanji, O. Stetzer, T. Tritscher, R. Chirico, M. F. Heringa, E. Weingartner, A. S. H. Prévôt, U. Baltensperger, and U. Lohmann (2013), Effect of photochemical ageing on the ice nucleation properties of diesel and wood burning particles, *Atmos. Chem. Phys.*, *13*(2), 761–772, doi:10.5194/acp-13-761-2013.

Cozic, J., S. Mertes, B. Verheggen, D. J. Cziczo, S. J. Gallavardin, S. Walter, U. Baltensperger, and E. Weingartner (2008), Black carbon enrichment in atmospheric ice particle residuals observed in lower tropospheric mixed phase clouds, *J. Geophys. Res.*, *113*, D15209, doi:10.1029/2007JD009266.

Creamean, J. M., K. J. Suski, D. Rosenfeld, A. Cazorla, P. J. DeMott, R. C. Sullivan, A. B. White, F. M. Ralph, P. Minnis, and J. M. Comstock (2013), Dust and biological aerosols from the Sahara and Asia influence precipitation in the western US, *Science*, *339*(6127), 1572–1578.

Cziczo, D. J., and K. D. Froyd (2014), Sampling the composition of cirrus ice residuals, *Atmos. Res.*, *142*(0), 15–31, doi:10.1016/j.atmosres.2013.06.012.

Cziczo, D. J., K. D. Froyd, S. J. Gallavardin, O. Moehler, S. Benz, H. Saathoff, and D. M. Murphy (2009), Deactivation of ice nuclei due to atmospherically relevant surface coatings, *Environ. Res. Lett.*, *4*(4), 044013, doi:10.1088/1748-9326/4/4/044013.

Cziczo, D. J., K. D. Froyd, C. Hoose, E. J. Jensen, M. Diao, M. A. Zondlo, J. B. Smith, C. H. Twohy, and D. M. Murphy (2013), Clarifying the dominant sources and mechanisms of cirrus cloud formation, *Science*, *340*(6138), 1320–1324, doi:10.1126/science.1234145.

DeMott, P. J., D. J. Cziczo, A. J. Prenni, D. M. Murphy, S. M. Kreidenweis, D. S. Thomson, R. Borys, and D. C. Rogers (2003), Measurements of the concentration and composition of nuclei for cirrus formation, *Proc. Natl. Acad. Sci. U.S.A.*, *100*(25), 14,655–14,660, doi:10.1073/pnas.2532677100.

DeMott, P. J., A. J. Prenni, X. Liu, S. M. Kreidenweis, M. D. Petters, C. H. Twohy, M. Richardson, T. Eidhammer, and D. Rogers (2010), Predicting global atmospheric ice nuclei distributions and their impacts on climate, *Proc. Natl. Acad. Sci. U.S.A.*, *107*(25), 11217–11222, doi:10.1073/pnas.0910818107.

DeMott, P. J., T. C. Hill, C. S. McCluskey, K. A. Prather, D. B. Collins, R. C. Sullivan, M. J. Ruppel, R. H. Mason, V. E. Irish, and T. Lee (2016), Sea spray aerosol as a unique source of ice nucleating particles, *Proc. Natl. Acad. Sci. U.S.A.*, *113*(21), 5797–5803, doi:10.1073/pnas.1514034112.

Dymarska, M., B. J. Murray, L. Sun, M. L. Eastwood, D. A. Knopf, and A. K. Bertram (2006), Deposition ice nucleation on soot at temperatures relevant for the lower troposphere, *J. Geophys. Res.*, *111*, D04204, doi:10.1029/2005JD006627.

Dzepina, K., et al. (2015), Molecular characterization of free tropospheric aerosol collected at the Pico Mountain Observatory: A case study with a long-range transported biomass burning plume, *Atmos. Chem. Phys.*, *15*(9), 5047–5068, doi:10.5194/acp-15-5047-2015.

Eastwood, M. L., S. Cremel, M. Wheeler, B. J. Murray, E. Girard, and A. K. Bertram (2009), Effects of sulfuric acid and ammonium sulfate coatings on the ice nucleation properties of kaolinite particles, *Geophy. Res. Lett.*, *36*, L02811, doi:10.1029/2008GL035997.

Friese, E., and A. Ebel (2010), Temperature dependent thermodynamic model of the system $H^+ - NH_4^+ - Na^+ - SO_4^{2-} - NO_3^- - Cl^- - H_2O$, *J. Phys. Chem. A*, *114*(43), 11,595–11,631, doi:10.1021/jp101041j.

Froyd, K. D., D. M. Murphy, P. Lawson, D. Baumgardner, and R. L. Herman (2010), Aerosols that form subvisible cirrus at the tropical tropopause, *Atmos. Chem. Phys.*, *10*(1), 209–218, doi:10.5194/acp-10-209-2010.

George, I. J., and J. P. D. Abbatt (2010), Heterogeneous oxidation of atmospheric aerosol particles by gas-phase radicals, *Nat. Chem.*, *2*(9), 713–722, doi:10.1038/nchem.806.

Heymsfield, A. J., and L. M. Miloshevich (1995), Relative humidity and temperature influences on cirrus formation and evolution: Observations from wave clouds and FIRE II, *J. Atmos. Sci.*, *52*(23), 4302–4326.

Hiranuma, N., S. D. Brooks, R. C. Moffet, A. Glen, A. Laskin, M. K. Gilles, P. Liu, A. M. Macdonald, J. W. Strapp, and G. M. McFarquhar (2013), Chemical characterization of individual particles and residuals of cloud droplets and ice crystals collected on board research aircraft in the ISDAC 2008 study, *J. Geophys. Res. Atmos.*, *118*, 6564–6579, doi:10.1002/jgrd.50484.

Honrath, R. E., R. C. Owen, M. Val Martín, J. S. Reid, K. Lapina, P. Fialho, M. P. Dziobak, J. Kleissl, and D. L. Westphal (2004), Regional and hemispheric impacts of anthropogenic and biomass burning emissions on summertime CO and O_3 in the North Atlantic lower free troposphere, *J. Geophys. Res.*, *109*, D24310, doi:10.1029/2004JD005147.

Hoose, C., U. Lohmann, R. Bennartz, B. Croft, and G. Lesins (2008), Global simulations of aerosol processing in clouds, *Atmos. Chem. Phys.*, *8*(23), 6939–6963.

Kamphus, M., M. Ettner-Mahl, T. Klimach, F. Drewnick, L. Keller, D. J. Cziczo, S. Mertes, S. Borrmann, and J. Curtius (2010), Chemical composition of ambient aerosol, ice residues and cloud droplet residues in mixed-phase clouds: single particle analysis during the Cloud and Aerosol Characterization Experiment (CLACE 6), *Atmos. Chem. Phys.*, *10*(16), 8077–8095, doi:10.5194/acp-10-8077-2010.

Kanakidou, M., et al. (2005), Organic aerosol and global climate modelling: A review, *Atmos. Chem. Phys.*, *5*(4), 1053–1123.

Kanji, Z. A., and J. P. Abbatt (2006), Laboratory studies of ice formation via deposition mode nucleation onto mineral dust and *n*-hexane soot samples, *J. Geophys. Res.*, *111*, D16204, doi:10.1029/2005JD006766.

Kanji, Z. A., O. Florea, and J. P. Abbatt (2008), Ice formation via deposition nucleation on mineral dust and organics: Dependence of onset relative humidity on total particulate surface area, *Environ. Res. Lett.*, *3*(2), 025004, doi:10.1088/1748-9326/3/2/025004.

Kanji, Z. A., A. Welti, C. Chou, O. Stetzer, and U. Lohmann (2013), Laboratory studies of immersion and deposition mode ice nucleation of ozone aged mineral dust particles, *Atmos. Chem. Phys.*, *13*(17), 9097–9118, doi:10.5194/acp-13-9097-2013.

Kärcher, B., and J. Ström (2003), The roles of dynamical variability and aerosols in cirrus cloud formation, *Atmos. Chem. Phys.*, *3*(3), 823–838, doi:10.5194/acp-3-823-2003.

Kaufmann, L., C. Marcolli, B. Luo, and T. Peter (2016a), Refreeze experiments of water droplets containing different types of ice nuclei interpreted by classical nucleation theory, *Atmos. Chem. Phys. Discuss.*, *2016*, 1–59.

Kaufmann, L., C. Marcolli, J. Hofer, V. Pinti, C. R. Hoyle, and T. Peter (2016b), Ice nucleation efficiency of natural dust samples in the immersion mode, *Atmos. Chem. Phys.*, *16*(17), 11,177–11,206.

Kleissl, J., R. E. Honrath, M. P. Dziobak, D. Tanner, M. Val Martín, R. C. Owen, and D. Helmig (2007), Occurrence of upslope flows at the Pico mountaintop observatory: A case study of orographic flows on a small, volcanic island, *J. Geophys. Res.*, *112*, D10S35, doi:10.1029/2006JD007565.

Knopf, D. A., and P. A. Alpert (2013), A water activity based model of heterogeneous ice nucleation kinetics for freezing of water and aqueous solution droplets, *Farad. Discuss.*, *165*, 513–534, doi:10.1039/C3FD00035D.

Knopf, D. A., and T. Koop (2006), Heterogeneous nucleation of ice on surrogates of mineral dust, *J. Geophys. Res.*, *111*, D12201, doi:10.1029/2005JD006894.

Knopf, D. A., and M. D. Lopez (2009), Homogeneous ice freezing temperatures and ice nucleation rates of aqueous ammonium sulfate and aqueous levoglucosan particles for relevant atmospheric conditions, *Phys. Chem. Chem. Phys.*, *11*(36), 8056–8068, doi:10.1039/B903750K

Knopf, D. A., B. Wang, A. Laskin, R. C. Moffet, and M. K. Gilles (2010), Heterogeneous nucleation of ice on anthropogenic organic particles collected in Mexico City, *Geophy. Res. Lett.*, *37*, L11803, doi:10.1029/2010GL043362.

Knopf, D. A., S. M. Forrester, and J. H. Slade (2011), Heterogeneous oxidation kinetics of organic biomass burning aerosol surrogates by O_3, NO_2, N_2O_5, and NO_3, *Phys. Chem. Chem. Phys.*, *13*(47), 21,050–21,062.

Knopf, D. A., P. A. Alpert, B. Wang, R. E. O'Brien, S. T. Kelly, A. Laskin, M. K. Gilles, and R. C. Moffet (2014), Microspectroscopic imaging and characterization of individually identified ice nucleating particles from a case field study, *J. Geophys. Res. Atmos.*, *119*, 10,365–10,381, doi:10.1002/2014JD021866.

Koop, T., and B. Zobrist (2009), Parameterizations for ice nucleation in biological and atmospheric systems, *Phys. Chem. Chem. Phys.*, *11*(46), 10,839–10,850, doi:10.1039/B914289D.

Koop, T., B. Luo, A. Tsias, and T. Peter (2000), Water activity as the determinant for homogeneous ice nucleation in aqueous solutions, *Nature*, *406*(6796), 611–614, doi:10.1038/35020537.

Koop, T., J. Bookhold, M. Shiraiwa, and U. Poschl (2011), Glass transition and phase state of organic compounds: Dependency on molecular properties and implications for secondary organic aerosols in the atmosphere, *Phys. Chem. Chem. Phys.*, *13*(43), 19,238–19,255, doi:10.1039/C1CP22617G.

Kroll, J. H., J. D. Smith, D. L. Che, S. H. Kessler, D. R. Worsnop, and K. R. Wilson (2009), Measurement of fragmentation and functionalization pathways in the heterogeneous oxidation of oxidized organic aerosol, *Phys. Chem. Chem. Phys.*, *11*(36), 8005–8014, doi:10.1039/B905289E.

Kulkarni, G., K. Zhang, C. Zhao, M. Nandasiri, V. Shutthanandan, X. Liu, J. Fast, and L. Berg (2015), Ice formation on nitric acid-coated dust particles: Laboratory and modeling studies, *J. Geophys. Res. Atmos.*, *120*, 7682–7698, doi:10.1002/2014JD022637.

Kulkarni, G., et al. (2016), Ice nucleation activity of diesel soot particles at cirrus relevant temperature conditions: Effects of hydration, secondary organics coating, soot morphology, and coagulation, *Geophy. Res. Lett.*, *43*, 3580–3588, doi:10.1002/2016GL068707.

Lau, K. M., and H. T. Wu (2003), Warm rain processes over tropical oceans and climate implications, *Geophy. Res. Lett.*, *30*(24, 2290), doi:10.1029/2003GL018567.

Lienhard, D. M., et al. (2015), Viscous organic aerosol particles in the upper troposphere: Diffusivity-controlled water uptake and ice nucleation?, *Atmos. Chem. Phys.*, *15*(23), 13,599–13,613, doi:10.5194/acp-15-13599-2015.

Marcolli, C. (2014), Deposition nucleation viewed as homogeneous or immersion freezing in pores and cavities, *Atmos. Chem. Phys.*, *14*(4), 2071–2104, doi:10.5194/acp-14-2071-2014.

Marcolli, C., B. Luo, and T. Peter (2004), Mixing of the organic aerosol fractions: Liquids as the thermodynamically stable phases, *J. Phys. Chem. A*, *108*(12), 2216–2224, doi:10.1021/jp036080l.

McFarquhar, G. M., G. Zhang, M. R. Poellot, G. L. Kok, R. McCoy, T. Tooman, A. Fridlind, and A. J. Heymsfield (2007), Ice properties of single-layer stratocumulus during the Mixed-Phase Arctic Cloud Experiment: 1. Observations, *J. Geophys. Res.*, *112*, D24201, doi:10.1029/2007JD008633.

Möhler, O., S. Benz, H. Saathoff, M. Schnaiter, R. Wagner, J. Schneider, S. Walter, V. Ebert, and S. Wagner (2008), The effect of organic coating on the heterogeneous ice nucleation efficiency of mineral dust aerosols, *Environ. Res. Lett.*, *3*(2), 025,007, doi:10.1088/1748-9326/3/2/025007.

Morrison, H., G. de Boer, G. Feingold, J. Harrington, M. D. Shupe, and K. Sulia (2012), Resilience of persistent Arctic mixed-phase clouds, *Nat. Geosci.*, *5*(1), 11–17, doi:10.1038/ngeo1332.

Mu, M., et al. (2011), Daily and 3-hourly variability in global fire emissions and consequences for atmospheric model predictions of carbon monoxide, *J. Geophys. Res.*, *116*, D24303, doi:10.1029/2011JD016245.

Mülmenstädt, J., O. Sourdeval, J. Delanoë, and J. Quaas (2015), Frequency of occurrence of rain from liquid-, mixed-, and ice-phase clouds derived from A-Train satellite retrievals, *Geophy. Res. Lett.*, *42*, 6502–6509, doi:10.1002/2015GL064604.

Murphy, D. M., and T. Koop (2005), Review of the vapour pressures of ice and supercooled water for atmospheric applications, *Q. J. R. Meteorol. Soc.*, *131*(608), 1539–1565, doi:10.1256/qj.04.94.

Murray, B. J. (2008), Inhibition of ice crystallisation in highly viscous aqueous organic acid droplets, *Atmos. Chem. Phys.*, *8*(17), 5423–5433.

Murray, B. J., T. W. Wilson, S. Dobbie, Z. Cui, S. M. Al-Jumur, O. Möhler, M. Schnaiter, R. Wagner, S. Benz, and M. Niemand (2010), Heterogeneous nucleation of ice particles on glassy aerosols under cirrus conditions, *Nat. Geosci.*, *3*(4), 233–237, doi:10.1038/ngeo817.

Murray, B. J., S. L. Broadley, T. W. Wilson, J. D. Atkinson, and R. H. Wills (2011), Heterogeneous freezing of water droplets containing kaolinite particles, *Atmos. Chem. Phys.*, *11*(9), 4191–4207.

Niemand, M., et al. (2012), A particle-surface-area-based parameterization of immersion freezing on desert dust particles, *J. Atmos. Sci.*, *69*(10), 3077–3092, doi:10.1175/JAS-D-11-0249.1.

Olivier, J. G. J., and J. J. M. Berdowski (2001), Global emissions sources and sinks, in *The Climate System*, A.A. Balkema Publishers/Swets & Zeitlinger Pub., Netherlands.

Owen, R. C., and R. E. Honrath (2009), Technical note: A new method for the Lagrangian tracking of pollution plumes from source to receptor using gridded model output, *Atmos. Chem. Phys.*, *9*(7), 2577–2595, doi:10.5194/acp-9-2577-2009.

Pitchford, M., W. Malm, B. Schichtel, N. Kumar, D. Lowenthal, and J. Hand (2007), Revised algorithm for estimating light extinction from IMPROVE particle speciation data, *J. Air Waste Manag. Assoc.*, *57*(11), 1326–1336, doi:10.3155/1047-3289.57.11.1326.

Pratt, K. A., P. J. DeMott, J. R. French, Z. Wang, D. L. Westphal, A. J. Heymsfield, C. H. Twohy, A. J. Prenni, and K. A. Prather (2009), In situ detection of biological particles in cloud ice-crystals, *Nat. Geosci.*, *2*(6), 398–401, doi:10.1038/ngeo521.

Pummer, B. G., et al. (2015), Ice nucleation by water-soluble macromolecules, *Atmos. Chem. Phys.*, *15*(8), 4077–4091.

Richardson, M. S., et al. (2007), Measurements of heterogeneous ice nuclei in the western United States in springtime and their relation to aerosol characteristics, *J. Geophys. Res.*, *112*, D02209, doi:10.1029/2006JD007500.

Schill, G. P., and M. A. Tolbert (2013), Heterogeneous ice nucleation on phase-separated organic-sulfate particles: Effect of liquid vs. glassy coatings, *Atmos. Chem. Phys.*, *13*(9), 4681–4695.

Schill, G. P., and M. A. Tolbert (2014), Heterogeneous ice nucleation on simulated sea-spray aerosol using Raman microscopy, *J. Phys. Chem. C*, *118*(50), 29,234–29,241.

Schill, G. P., D. O. De Haan, and M. A. Tolbert (2014), Heterogeneous ice nucleation on simulated secondary organic aerosol, *Environ. Sci. Technol.*, *48*(3), 1675–1682.

Seibert, P., and A. Frank (2004), Source-receptor matrix calculation with a Lagrangian particle dispersion model in backward mode, *Atmos. Chem. Phys.*, *4*(1), 51–63.

Song, F., and Y. Gao (2009), Chemical characteristics of precipitation at metropolitan Newark in the US East Coast, *Atmos. Environ.*, *43*(32), 4903–4913, doi:10.1016/j.atmosenv.2009.07.024.

Stohl, A., C. Forster, A. Frank, P. Seibert, and G. Wotawa (2005), Technical note: The Lagrangian particle dispersion model FLEXPART version 6.2, *Atmos. Chem. Phys.*, *5*(9), 2461–2474, doi:10.5194/acp-5-2461-2005.

Sullivan, R., M. Petters, P. DeMott, S. Kreidenweis, H. Wex, D. Niedermeier, S. Hartmann, T. Clauss, F. Stratmann, and P. Reitz (2010), Irreversible loss of ice nucleation active sites in mineral dust particles caused by sulphuric acid condensation, *Atmos. Chem. Phys.*, *10*(23), 11,471–11,487, doi:10.5194/acp-10-11471-2010.

Tobo, Y., A. J. Prenni, P. J. DeMott, J. A. Huffman, C. S. McCluskey, G. Tian, C. Pöhlker, U. Pöschl, and S. M. Kreidenweis (2013), Biological aerosol particles as a key determinant of ice nuclei populations in a forest ecosystem, *J. Geophys. Res. Atmos.*, *118*, 10,100–110,110, doi:10.1002/jgrd.50801.

Twohy, C. H., and M. R. Poellot (2005), Chemical characteristics of ice residual nuclei in anvil cirrus clouds: Evidence for homogeneous and heterogeneous ice formation, *Atmos. Chem. Phys.*, *5*(8), 2289–2297, doi:10.5194/acp-5-2289-2005.

Wagner, R., O. Möhler, H. Saathoff, M. Schnaiter, J. Skrotzki, T. Leisner, T. W. Wilson, T. L. Malkin, and B. J. Murray (2012), Ice cloud processing of ultra-viscous/glassy aerosol particles leads to enhanced ice nucleation ability, *Atmos. Chem. Phys.*, *12*(18), 8589–8610.

Wang, B., and D. A. Knopf (2011), Heterogeneous ice nucleation on particles composed of humic-like substances impacted by O_3, *J. Geophys. Res.*, *116*, D03205, doi:10.1029/2010JD014964.

Wang, B., A. T. Lambe, P. Massoli, T. B. Onasch, P. Davidovits, D. R. Worsnop, and D. A. Knopf (2012a), The deposition ice nucleation and immersion freezing potential of amorphous secondary organic aerosol: Pathways for ice and mixed-phase cloud formation, *J. Geophys. Res.*, *117*, D16209, doi:10.1029/2012JD018063.

Wang, B., A. Laskin, T. Roedel, M. K. Gilles, R. C. Moffet, A. V. Tivanski, and D. A. Knopf (2012b), Heterogeneous ice nucleation and water uptake by field-collected atmospheric particles below 273 K, *J. Geophys. Res.*, *117*, D00V19, doi:10.1029/2012JD017446.

Wex, H., P. DeMott, Y. Tobo, S. Hartmann, M. Rösch, T. Clauss, L. Tomsche, D. Niedermeier, and F. Stratmann (2014), Kaolinite particles as ice nuclei: Learning from the use of different kaolinite samples and different coatings, *Atmos. Chem. Phys.*, *14*(11), 5529–5546.

Wilson, T. W., et al. (2012), Glassy aerosols with a range of compositions nucleate ice heterogeneously at cirrus temperatures, *Atmos. Chem. Phys.*, *12*(18), 8611–8632, doi:10.5194/acp-12-8611-2012.

Wise, M. E., K. J. Baustian, and M. A. Tolbert (2010), Internally mixed sulfate and organic particles as potential ice nuclei in the tropical tropopause region, *Proc. Natl. Acad. Sci. U.S.A.*, *107*(15), 6693–6698.

Wise, M. E., K. J. Baustian, T. Koop, M. A. Freedman, E. J. Jensen, and M. A. Tolbert (2012), Depositional ice nucleation onto crystalline hydrated NaCl particles: A new mechanism for ice formation in the troposphere, *Atmos. Chem. Phys.*, *12*(2), 1121–1134, doi:10.5194/acp-12-1121-2012.

Zhang, B., R. C. Owen, J. A. Perlinger, A. Kumar, S. Wu, M. V. Martin, L. Kramer, D. Helmig, and R. E. Honrath (2014), A semi-Lagrangian view of ozone production tendency in North American outflow in the summers of 2009 and 2010, *Atmos. Chem. Phys.*, *14*(5), 2267–2287, doi:10.5194/acp-14-2267-2014.